RSC Advances

PAPER

View Article Online
View Journal | View Issue

Cite this: *RSC Adv.*, 2020, **10**, 36873

Performance of the dye-sensitized quasi-solid state solar cell with combined anthocyanin-ruthenium photosensitizer†

Eka Cahya Prima,[a] Harbi Setyo Nugroho,[b] Nugraha,[bc] Gema Refantero,[b] Camelia Panatarani[d] and Brian Yuliarto *[bc]

This work contributes to combining 12.2 mM purified anthocyanin of cyanidin-3-glucoside extracted from Indonesian black rice as the natural pigment with a ruthenium photosensitizer (1 : 1) in dye-sensitized solar cells (DSSCs) in liquid and quasi solid-state electrolytes. The findings essentially highlight the spectroscopic and electron transfer mechanism for the future trend of D–π–A natural pigment modification. The complete pigment comparison, dye absorbance, dye adsorption onto the semiconductor, dye electronic properties, electron excitation, and regeneration were investigated using spectroscopic methods. Cells employ TiO_2 mesoporous nanoparticles (19.18 nm grain size, 50.99 m^2 g^{-1} surface area, 87.8% anatase 12.2% rutile, 10.58 μm thickness, 3.18 eV band gap) sensitized by anthocyanin-N719 photosensitizer (12.2 mM) with the I^-/I_3^- electrolyte (0.1 M lithium iodide/0.05 M iodine/0.6 M 1-buty-3-methylimidazolium iodide/0.5 M 4-*tert*-butylpyridine/polyethylene oxide $M_w = 1 \times 10^6$) – Pt film. As a result, the quasi-solid state with combined anthocyanin-ruthenium dye-sensitized solar cell (3.51%) is achieved and reported for the first time. The work also achieved the highest efficiency of the anthocyanin dye-sensitized quasi-solid state solar cells of 2.65%. The insight on how the combined anthocyanin-N719 and the quasi-solid state electrolytes exhibit better performances will be further discussed.

Received 29th July 2020
Accepted 15th September 2020

DOI: 10.1039/d0ra06550a

rsc.li/rsc-advances

1. Introduction

Dye-sensitized solar cells (DSSCs) have attracted considerable attention for the future generation of solar cells with a wide area of application such as window glass, car windshields, mobile chargers, or flexible and transparent solar cells due to their abundant, non-toxic, low-cost, and renewable sources.[1,2] The natural dyes in DSSCs are obtained from organic sources such as anthocyanin, chlorophyll, betalain, and carotenoid.[3] The dye absorber materials are bonded to the TiO_2 porous material in order to broaden the semiconductor film absorbance. The electron is injected from the dye absorber materials into the n-type semiconductor during the illumination, and then a hole is left on the surface-absorbed dye ion.[4] Due to the wide band gap and large surface area, TiO_2 nanoparticles are used as photoelectrodes in this solar cell system.[5]

The optimization of DSSC has become an attractive research interest for the further development of renewable energy due to abundant, low-cost, and renewable sources. One of key aims of DSSC development is to enhance the electron transferability. In comparison to the standard organometallic pigments based on the ruthenium (N719) material complexes, the electron transferability of the natural pigment remains lower even though the natural pigment has higher absorbance than that of N719.[6] The molar extinction coefficient of anthocyanin dye is 26 900 M^{-1} cm^{-1} at 550 nm, whereas that of the N719 photosensitizer is 14 000 M^{-1} cm^{-1} at 515 nm.[7–9] Therefore, different methods are applied in this work so as to enhance the performance of natural photosensitizers such as dye combination,[1,10–13] dye purification,[14–18] and electrolyte layer modification.[19–21]

The development of natural photosensitizers based on anthocyanin has become an attractive topic due to the hydroxyl group-containing pigment, which facilitates proper dye attachment.[22,23] Kimura and co-workers explored the use of five single anthocyanin derivatives as purified dye photosensitizers.[22] The best device with an efficiency of 1.42% in MeOH solvent was obtained using Pg3G as the dye photosensitizer. Another work by a different research group revealed that long-hydroxyl and carbonyl-chain bearing anthocyanin generates maximum electron transfer rate ($\kappa_{\varepsilon T}$) and results in the highest efficiency of 1.87% for anthocyanin with a concentration of 1 g dye per 10 mL water.[24] The use of pomegranate dye has been reported by

[a]*Department of Science Education, Faculty of Mathematics and Science Education, Universitas Pendidikan Indonesia, Bandung, Indonesia*

[b]*Department of Engineering Physics, Faculty of Industrial Technology, Institut Teknologi Bandung, Bandung, Indonesia. E-mail: brian@tf.itb.ac.id*

[c]*National Research Center of Nanotechnology (NRCN), Institut Teknologi Bandung, Bandung, Indonesia*

[d]*Department of Physics, Faculty of Mathematics and Natural Science, Universitas Padjadjaran, Bandung, Indonesia*

† Electronic supplementary information (ESI) available. See DOI: 10.1039/d0ra06550a

Ghann *et al.*, which successfully narrowed the band gap, and as a result, the power conversion efficiency of 2.0% was obtained.[11] The use of four synthetic environment-friendly flavylium salts as anthocyanin-like sensitizers has been reported by Calogero *et al.*[25] In our previous work, we investigated the pigments of single and combined cyanidin-3-*O*-glucoside and peonidin-3-*O*-glucoside with a concentration of 2.0 mM and pH 2.0.[1] Experimental and theoretical investigations were done to broaden the understanding of how the combination of these pigments contributes to the electronic structure and the photochemical performance of the DSSC.

Natural DSSC photosensitizer studies have shown a novel trend for improving the natural pigment performance by modifying the D–π–A structure.[26,27] Regardless of the contamination by toxic materials of the ruthenium pigment and the non-toxic materials of the natural pigment, the low natural performance needs to be improved due to the lack of absorbance, adsorption, and electron transfer ability compared to the standard organometallic pigments based on ruthenium complex materials. Although the previously established N719/TiO_2 cell has achieved an efficiency 11.1%,[28] we are concerned about benchmark natural pigments with N719. By studying and comparing these pigments, we believe that the findings will contribute to the development of novel modified natural photosensitizer pigments for future natural dye-sensitized solar cells. However, there is no complete head-to-head comparison between the natural sensitizer and N719 pigment, although this information is very fundamental for developing the natural pigment as a low-cost material with high efficiency. Interestingly, in comparison with N719, the molar extinction coefficient of anthocyanin dye is 26 900 M^{-1} cm^{-1} at 550 nm, whereas that of the N719 photosensitizer is 14 000 M^{-1} cm^{-1} at 515 nm.[16,18,29] Luo *et al.* reported the co-sensitized dithiafulvenyl-phenothiazine (DTF-PTZ)-based organic dyes with N719 for improving the performance of the DSSC.[7] The DTF-PTZ and N719 co-sensitized DSSC showed significant improvement by about 3%. A different work by Liu *et al.* reported the combined PbS-N719 dye-sensitized material to improve the performance of the DSSC.[30] This combination has elevated the open-circuit voltage (V_{OC}) and increased the device efficiency from 5.95% to 6.35%. To the best of our knowledge, we have reported the combined anthocyanin-N719 photosensitizer in quasi-solid state dye-sensitized solar cells for the first time.

Lately, the discussion of a liquid *versus* quasi-solid state electrolyte for DSSC has attracted research interest due to its unique properties.[20,31] Quasi-solid state electrolytes have the features of solids such as definite shape and volume. Nevertheless, they also have liquid properties such as high ionic conductivity and better interfacial contact with the mesoporous photoanode. Unfortunately, DSSC based on quasi-solid electrolyte tend to generate lower efficiency compared to liquid electrolyte-based DSSC due to poorer ion diffusion and sub-optimal interfacial contact with the mesoporous layer.[32] Although the use of liquid electrolytes usually shows better ionic conductivity, the treatment also leads to several problems concerning solar cell sealing and manufacturing such as electrolyte leakage, volatilization, desorption of the adsorbed photosensitizers, and corrosion of the counter electrode, which contribute to instability during long-term usage.[31] For these reasons, the utilization of quasi-solid state electrolytes has interested researchers to optimize the performance of DSSC.

Regarding the quasi solid-state electrolyte for natural pigment-based DSSC assembly, the problem of quasi solid-state electrolyte penetration through the dye-adsorbed TiO_2 has been treated by providing the preheated quasi solid-state electrolyte before insertion into the cell sandwich. The semi-liquid phase of the electrolyte facilitates the electrolyte to penetrate through the semiconductor before being dry as a gel. In this work, the quasi-solid state electrolyte has been compared to the liquid electrolyte with the same I^-/I_3^- concentration ratio. 0.6 M 1-buty-3-methylimidazolium iodide (BMII) and 0.5 M 4-*tert*-butylpyridine (TBP) have been employed as the stabilizing additives for the LiI/I_2-based electrolyte in acetonitrile solution. The quasi-solid state electrolyte has been prepared based on the polyethylene oxide polymer ($M_w = 1 \times 10^6$).

The characterization was performed by the spectroscopic methods in order to consistently compare the performance of the anthocyanin-N719 pigment, including the absorbance, adsorption, electronic properties, energy efficiency, and charge transfer properties. Fourier transform infrared (FTIR) analysis was performed to analyze the molecular vibration of the dye photosensitizer. UV-Vis spectroscopy was performed to investigate the dye's absorbance. Cyclic voltammetry was performed to analyze the redox potentials. Also, the oxidation potential, the reduction potential, the HOMO–LUMO orbitals, and the gap energy were included in the potential redox analysis.[39] The *I–V* characteristics were studied to analyze the low current density (J_{SC}), the open-circuit voltage (V_{OC}), the fill factor (FF), and the power conversion efficiency (η). Moreover, the electron injection investigation was also performed using several electrochemical impedance spectroscopy (EIS) parameters such as the diffusion resistance (R_d), recombination resistance (R_r), diffusion lifetime (τ_d), recombination lifetime (τ_n), diffusion rate (D_n), chemical capacitance ($C_{\mu elec}$), and conductivity (σ_n).

2. Materials and methods

2.1 Preparation of the photosensitizers

Indonesian black rice (*Oryza sativa* L.) pigment was extracted and purified to obtain cyanidin-3-*O*-glucoside anthocyanin photosensitizers. The black rice grains were firstly dried and ground to prepare black rice powder. Unpurified anthocyanin extract was prepared by adding 200 g black rice powder into a solution and then stirring it at 800 rpm at the temperature of 50 °C for 2.5 hours. The solution was previously prepared by stirring together 400 mL methanol and 5 mL hydrochloric acid in 95 mL distilled water for 5 minutes under room temperature. The mixture was then macerated for three weeks at room temperature in dark conditions. The mixture was then filtered using a vacuum pump through 110 mm Whatman's filter paper after previously centrifuging it at 4000 rpm for 30 minutes. The extract was then poured into 50 mL aluminum-coated glass and placed in a refrigerator at 5 °C to store the pigment. Then, the extract was evaporated at 40 °C for two days in a darkroom and

vacuum conditions to obtain 4.5 g of the unpurified anthocyanin powder. The anthocyanin concentration was measured using eqn (1). Moreover, it was then adjusted by diluting a similar solvent.[18,30]

$$\text{Anthocyanin concentration (mg L}^{-1}) = A \times \text{MW} \times \text{DF} \times 10^3/\varepsilon \times l \quad (1)$$

where MW is the molecular weight of about 449.3 g mol^{-1}, DF is the factor of dilution, ε is the coefficient of molar extinction, which equals to 26 900 M^{-1} cm^{-1} relative to the cyanidin-3-glucoside, l is the 1 cm light-path length, and A is the absorbance given by eqn (2).

$$A = (A_{max} - A_{700})_{pH\ 1} - (A_{max} - A_{700})_{pH\ 4.5} \quad (2)$$

The dye's pH was adjusted by diluting the 0.025 M potassium chloride buffer solution to result in pH 1.0 and 0.4 M sodium acetate to result in pH 4.5. The particular buffer solution was diluted by 225 mL H_2O, and pH was adjusted to 1.0 and 4.5 by adding hydrochloric acid dropwise. Next, the purification of the unpurified anthocyanin powder was done to separate cyanidin-3-glucoside and peonidin-3-glucoside using the standardized method previously reported by Park *et al.* and Ordaz-Galindo *et al.*[18,33] The method was carried out by dissolving the unpurified anthocyanin powder in 15 mL *n*-hexane and then pouring it into an Amberlite XAD-7 Aldrich® calibrated chromatography column with the solvent reservoir. The polar constituents were removed by eluting the column with 15 mL HCl 0.3% and then the solution was sequentially eluted using 10 : 90, 20 : 80, 30 : 70, and 40 : 60 vol% methanol : water containing HCl 0.3%. Precoated RP-18 F_{254s} thin-layer chromatography (TLC) plate (0.25 mm layer thickness) was then used to test the isolated anthocyanin extract with 10 : 90 vol% methanol : water containing HCL 0.3% to analyze the XAD-7 Aldrich®-calibrated chromatography column fractions.[34,35] The detailed analysis of anthocyanin concentration can be found in the ESI in Fig. S3–S5.† The purification provided 3.06 g cyanidin-3-glucoside and 0.27 g peonidin-3-glucoside. In this work, cyanidin-3-glucoside has been subsequently named as anthocyanin. Finally, the combined anthocyanin-N719 dye-photosensitizer was prepared by mixing purified anthocyanin and N719 in the stoichiometric ratio of 1 : 1 in a solution containing 19 mL H_2O, 80 mL MeOH, and 1 mL HCl, resulting in 12.2 mM pigment concentration with pH 1.0 in all the cases.

2.2 Preparation of liquid and quasi solid-state electrolytes

The liquid-state electrolyte was prepared by mixing 0.1 M lithium iodide (LiI) and 0.05 M iodine (I_2) in 100 mL acetonitrile. The solution was then stirred at 300 rpm for 5 minutes until a well-mixed solution was formed. Next, 0.6 M 1-buty-3-methylimidazolium iodide (BMII) and 0.5 M 4-*tert*-butylpyridine (TBP) were added and stirred overnight. The electrolyte was then poured into a dark bottle and placed at room temperature. Afterwards, the electrolyte solution was ready to use as a liquid-state electrolyte mediator for DSSC containing I^-/I_3^-. Finally, the quasi-solid electrolyte was prepared by mixing 10 mL electrolyte solution and 2 g polyethylene oxide ($M_w = 1 \times 10^6$). This mixture was then stirred at room temperature for 24 hours until it became a quasi-solid state. The quasi-solid state electrolyte was maintained at 60 °C before being attached to the dye-adsorbed TiO_2.

2.3 Preparation of the Surlyn spacer

The Surlyn polymer was cut to have an area of 2 × 2 cm^2 with 25 μm thickness in order to prepare the sealant material. The inside spacer hole was also cut to have an area of 0.7 × 0.7 cm^2 so as to make the film frame. The cell was assembled after uncovering the thicker plastic from the sealant material and then the two sealants were clipped to each other. Lastly, the spacer was cleaned using isopropyl alcohol.

2.4 Preparation of TiO_2 nanoparticle photoelectrode and Pt-Counter electrode

The TiO_2 nanoparticle film was prepared using the sol–gel method. First, the solvent solution was prepared by stirring 30 mL acetic acid and 30 mL water at 600 rpm for 5 minutes. 5 g titanium dioxide P25 and 1.5 g polyethylene glycol (PEG, molecular weight = 20 000) as a polymer was added into the solution and stirred at 600 rpm for 3 hours. This material was used to prevent agglomeration. A few drops of the Triton X-100 surfactant were added to the solution. Moreover, few drops of hydrochloric acid were also added to the paste so as to adjust the pH to 1.0. This treatment has a vital role in improving the number of anatase phases and the stability of TiO_2 nanoparticles, following the previous work by Chae, *et al.*[36] This evidence was supported by Tryba *et al.*, who found that under acidic conditions, TiO_2 nanoparticles possessed the most crystallized anatase phase in comparison to the others, although this treatment did not contribute to the enlargement of the surface area of the particles.[37]

Furthermore, the solution was heated and kept at 80 °C with 600 rpm stirring. Sonication treatment was applied for 3 hours to obtain the uniform TiO_2 paste for further TiO_2 film preparation. The TiO_2 paste was then spin-coated onto fluorine-doped tin oxide (FTO) glass at 4000 rpm for 30 seconds. The FTO glass has an area of 2 × 2.5 cm^2 with a frame size of 0.5 × 0.5 cm^2 and a sheet resistance of 8 Ω per sq. The TiO_2 film photoelectrode with a film area of 0.25 cm^2 was fabricated using the spin-coating process, as seen in the ESI in Fig. S7.† The spin-coating process was repeated twice to obtain the desired thickness of about 10.58 μm. The film was then heated using a three-stage temperature gradient from 125 °C for 15 minutes, 325 °C for 15 minutes, and 450 °C for 30 minutes with the heating rate of 2 °C per minute.

The dye photosensitizers were then deposited onto the TiO_2 film photoelectrode by soaking the TiO_2 film photoelectrode in the dye solution for four days. In this work, we prepared three different dye solutions with the same concentration of 12.2 mM and volume of 10 mL, namely, anthocyanin, anthocyanin-N719 (1 : 1), and N719; hence, we present three different variations of the dye absorber. After the soaking process, the loose pigments were then removed from the TiO_2 film photoelectrode using

isopropyl alcohol. To evaluate the dye adsorption, we analyzed the pigment concentration before and after dye adsorption. All the film glasses were immersed in the pigments. Regardless of the small amount of pigment adsorption on FTO when we removed the films from the dyes, we assumed that the pigment was predominantly adsorbed onto the TiO_2 film. The dye before and after adsorption was diluted 50 times with the same solvent so as to investigate it using UV-Vis spectroscopy, as reported in Fig. 7. The counter electrode film was then prepared by cleaning it using acetone, 2-propanol, and water, followed by drying at 60 °C. The Pt layer was sputtered as the counter electrode film under a pressure and applied current of 10 Pa and 20 mA, respectively; the film was calcined at 300 °C for 30 minutes.

2.5 DSSC assembling

The devices were then completed by sandwiching the dye-absorbed TiO_2 film and the Pt-sputtered film with the insertion of the I^-/I_3^- electrolyte and sealing with the prepared Surlyn frame. Besides, two different electrolyte states, namely, the liquid state and the quasi-solid state, were prepared in this work. We present six different samples with the variation of the dyes and the electrolyte state: (a) anthocyanin with the liquid-state electrolyte, (b) anthocyanin with the quasi-solid state electrolyte, (c) anthocyanin-N719 with the liquid-state electrolyte, (d) anthocyanin-N719 with the quasi-solid state electrolyte, (e) N719 with the liquid-state electrolyte, and (f) N719 with the quasi-solid state electrolyte. Each sample was inserted by the 25 μm Surlyn polymer, as described before, clipped on the four sides of the sandwiched film, and then put under a 350 nm UV lamp for 30 seconds. Subsequently, the samples were put on a hotplate and then dried at 100 °C for 60 seconds. Finally, the samples were cooled under room temperature and were then ready to conduct the characterization and measurements.

2.6 Characterization and measurements

Spectroscopic studies were used for the investigation in this work. A FT/IR Jasco-6100, Japan, equipped with a potassium bromide (KBr) plate with scanning range from 400 to 4500 cm^{-1}, was used for the spectroscopic analysis, the binding vibrations of the organic molecule in solution. A UV-Vis spectrophotometer from Hewlett Packard 8453 Agilent Technologies and a Jasco V-670 Spectrophotometer were used to check the dye's absorbance. A Hitachi S-4800 FE-SEM was used to study the morphology and the thickness of the photoanode coatings. The NMR spectra were recorded on a JEOL JNM-ECP500 (^{1}H: 500 MHz). The anthocyanin NMR analysis referred to the previous finding by Fernandes *et al.*, Lee, and Park *et al.*[33,38,40] The eDAQ potentiostat is equipped with an e-coder 401, software Echem Ver. 2.1, and the scan rate of 50 mV s^{-1}, the range of −1.8 V to +1.8 mV, and the positive initial direction was used for cyclic voltammetric measurements. The three electrodes used were a platinum counter electrode, a glassy carbon electrode, and an Ag/AgCl reference in 3 M NaCl solution as the reference electrode. The electrolyte used was 0.1 M tetrabutylammonium tetrafluoroborate $(n\text{-}C_4H_9)_4NPF_6$ in acetonitrile as the supporting electrolyte. The empirical Bredas equation was estimated to determine the HOMO position based on the onset curve of voltammetry.[41] The dye's highest occupied molecular orbital (HOMO) is given by eqn (3).

$$E_{HOMO} = -e(E_{ox}^{onset} + 4.4) \quad (3)$$

The E_{ox}^{onset} data is plotted from the oxidation potential voltammetry measured by the eDAQ potentiostat. The dyes' direct energy gaps were calculated from the UV-Vis spectral data using Tauc's Relation, as estimated in eqn (4).[42]

$$\alpha hv \approx (hv - E_g)^n \quad (4)$$

The dyes' direct band gaps (E_g) were obtained from the α extrapolation to 0 when $n = 2$. On the other hand, E_g is the dye's band gap, α is the dye's absorbance, and hv is the photon energy. The absorbance data was be used to obtain the band gap and light-harvesting efficiency (LHE) of the absorber layer of each sample. The band gap was obtained using the Tauc plot method and LHE was obtained using eqn (5).[43]

$$LHE(\lambda) = (1 - 10^{-\infty}) \times 100\% \quad (5)$$

where α is the absorbance; since the LHE is proportional to an incident photon to current efficiency (IPCE), the characterization of TiO_2 nanoparticles was done using X-ray diffraction, scanning electron microscopy, and Brunauer–Emmett–Teller (BET) analysis. A Rigaku Ultima IV X-ray diffractometer with Cu radiation (λ = 0.154056 nm) was used to obtain the X-ray diffraction pattern. A Hitachi S-4800 scanning electron microscope was used to characterize the surface and cross-section of the TiO_2 nanoparticles. A Thermo Plus EVO2 was used to carry out the thermogravimetric-differential thermal analysis (TG-DTA); 28.479 mg of the TiO_2 sample was used to carry out TG-DTA heated from 25 °C until 550 °C with a heating rate of 10 °C per minute. Al_2O_3 was used as the reference. The grain size of TiO_2 was calculated by Scherrer's equation, as expressed in eqn (6).

$$D = \frac{K\lambda}{\beta \cos \theta} \quad (6)$$

where D is the average TiO_2 crystallite size, K is the dimensionless shape factor (0.9 for the spherical particles), λ is the Cu Kα X-ray radiation wavelength of 0.1540598 nm, and β is the full width at half-maximum height for the diffraction peak of 0.007406 based on the XRD peak of TiO_2 for the plane of (101) at the 2θ of 25.26°. The phase identification of TiO_2 nanoparticles was performed using the Match Software version 3.8.1.143. A Micromeritics VacPrep 061 was used to analyze the photoelectrode surface area. The adsorptive analysis used N_2 gas, with the bath temperature of 77.350 K, sample mass of 0.1710 g, and cold free space of 29.0507 cm^3. The *J–V* characterization was performed under standard test conditions (AM 1.5G, 100 mW cm^{-2}) using a solar simulator calibrated with a Precision Spectral Pyranometer (MS-402F, Eiko-Seiki, Japan) and a 500 W Xenon lamp (Oriel, USA). The *J–V* curve was then plotted using a Keithley (4200-SCS) meter. The *J–V* curve was used to determine the short current density (J_{SC}), the open-circuit voltage

(V_{OC}), and the FF (Fill Factor). The fill factor (FF) was calculated based on the data from the J–V curve using the relation FF = $(J_{max}V_{max})/(J_{SC}V_{OC})$. Hence, the power conversion efficiency of the device could be determined using $\eta = (J_{SC}V_{OC}FF)/(\text{power density})$. The Gamry Instrument Reference 3000 Potentiostat/Galvanostat/ZRA and the EIS300 software for electrochemical impedance spectroscopy were used for the EIS measurement of the device. The analysis of electrochemical impedance was done by applying a forward bias and alternating current voltage amplitude of 0.70 V and 10.0 mV, respectively.[44] The details of the EIS parameter calculation can be seen in the ESI.† The frequency response was scanned from 200 mHz through 1 MHz. The Z-View software (v3.3e, Scribner Associate Inc.) was used to estimate the equivalent circuits and impedance parameters by fitting the spectra. The well-developed EIS method by Bisquert's group was used to investigate the electron transfer properties of the photosensitizer.[45–50] The complete EIS analysis of the combined anthocyanin-N719 DSSC is described in the ESI.†

3. Results and discussion

Fig. 1 describes the Thermo Gravimetric-Differential Thermal Analysis (TG-DTA) results for TiO_2 P25. From the TGA curve, when the sample was heated up to 125 °C, there was a dramatic weight loss of about 70.8% due to the hydroxyl (–OH) group solvent evaporation from acetic acid and water.[51] The second region between 125–325 °C was attributed to organic decomposition. As the temperature was increased up to 420 °C, the weight loss was due to residual polymer oxidation and decomposition of chlorine (obtained from hydrochloric acid) bonded to Ti–OH.[51] The TGA curve also shows that the residual polymer was removed entirely at calcination temperatures above 450 °C. As the temperature increased up to 500 °C, the weight loss was about 86.55%.

The DTA curve clearly presents two peaks, an endothermic peak in the region of 100–250 °C, which is assigned to solvent evaporation, and a broad exothermic peak at about 325 °C–420 °C, which is assigned to the decomposition of the chlorine, the polymer, and the phase transformation from amorphous to TiO_2 anatase. The phase transformation starts from 325 °C.[51] As shown in the full TG-DTA curve, the data from the TGA curve directly corresponds to the DTA record because the endothermic or the exothermic processes are always accompanied by weight loss.

Fig. 2 depicts the X-ray diffraction pattern of TiO_2 nanoparticles compared to the standard anatase and rutile peaks from JCPDS 21-1272 and 21-1276, respectively. The graph indicates that TiO_2 nanoparticles result in the structure of mixed anatase and rutile. The photoelectrode contains 87.8% anatase, as confirmed by the diffraction peaks at (101), (103), (200), (105), and (211), which respectively appear at the 2θ of 25.30°, 37.78°, 47.98°, 51.58°, and 55.02°, respectively. The semiconductor also contains 12.2% rutile phase, as confirmed by the diffraction peaks at (110), (101), (200), (111), (210), (211), and (220), which respectively appear at 2θ of 27.51°, 36.04°, 39.31°, 41.19°, 44.14°, 54.23°, and 56.78°. According to the grain size calculation corresponding to all the planes using Scherrer's equation on the plane of (101), the average particle size is approximately 19.185 nm. A smaller crystallite size of the particles will facilitate a higher number of dye molecules attaching the TiO_2 film. Moreover, the band gap analysis of TiO_2 shows that the film has a 3.18 eV optical TiO_2 band gap.

Fig. 3 shows the scanning electron microscopy (SEM) images of TiO_2 nanoparticles. According to Fig. 3(a), it can be seen that the film thickness influences the number of pigment attachments in contrast to the electron transports. Therefore, the TiO_2 photoelectrode has been adjusted to the film thickness of 10.58 μm according to the previously optimized result.[6] Fig. 3(e) also displays that the Pt film has a thickness of 0.59 μm. The TiO_2 images in Fig. 3(a–c) show that the TiO_2 nanoparticles have a unique mesoporous morphology. The mesoporous morphology facilitates the dyes to adsorb as well as redox couple (I^-/I_3^-) penetration into the film. The average grain size obtained from the SEM image is about 24.62 nm. The surface analysis of TiO_2 nanoparticles conducted using the Brunauer–Emmett–Teller (BET) method demonstrates the graph of the isothermal linear plot of the adsorption–desorption of N_2 gas surrounding the TiO_2 nanoparticles and the pore size

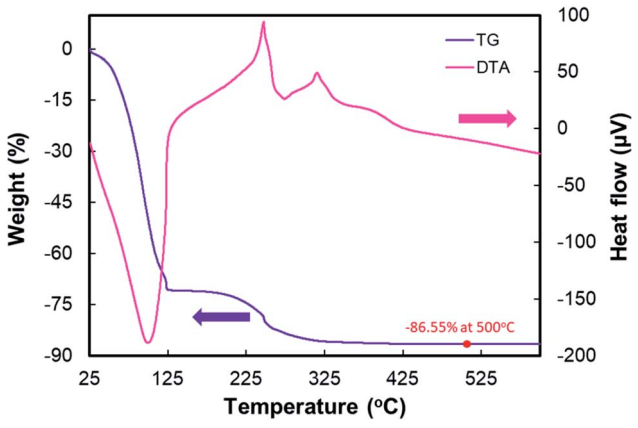

Fig. 1 TG-DTA results for TiO_2 nanoparticles.

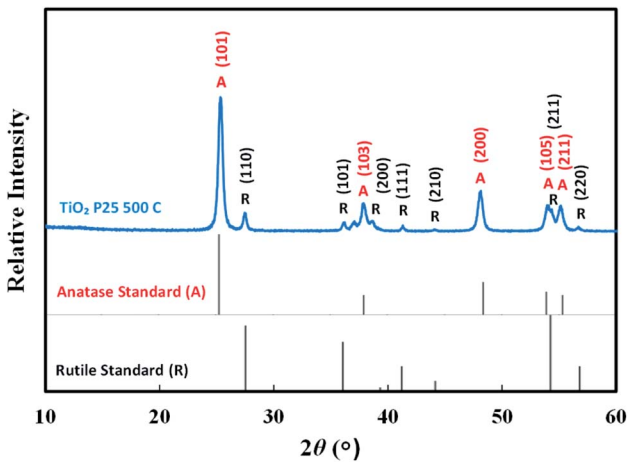

Fig. 2 X-ray diffraction pattern of TiO_2 nanoparticles containing anatase and rutile phases.

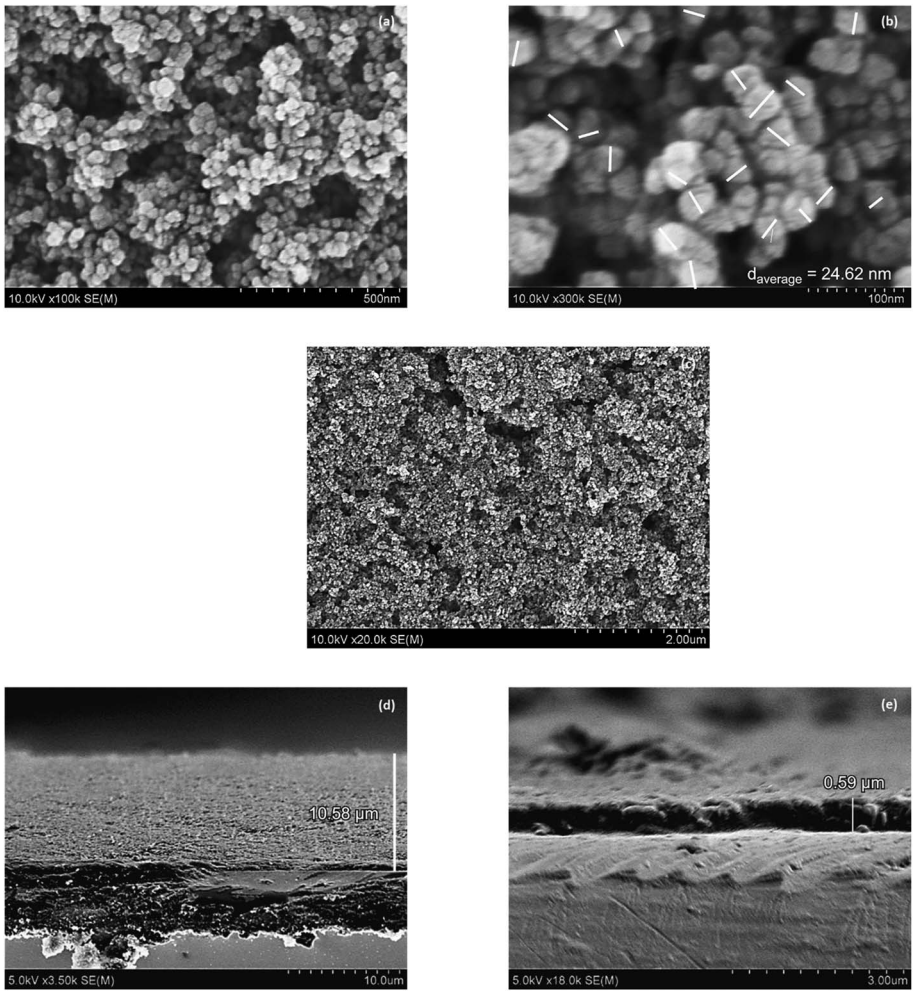

Fig. 3 The scanning electron microscopy (SEM) images of (a) the surface of TiO_2 nanoparticles with 100 000 times magnification, (b) 300 000 times magnification, (c) 20 000 times magnification, (d) the cross-section area of TiO_2, (e) the cross-section area of the Pt film.

distribution curves, as seen in Fig. 4. The sample demonstrated the isotherm of type IV (BDDT classification) with the H3 hysteresis loop type in the relative pressure range of 0.86–1.0. The result shows the existence of a mesoporous structure. The average surface area of the TiO_2 nanoparticles is 50.9931 m^2 g^{-1}.

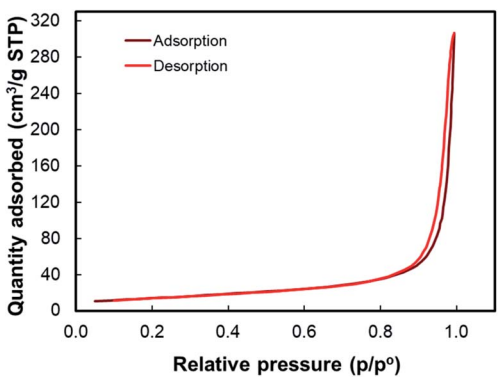

Fig. 4 Adsorption–desorption isotherm for the BET analysis of TiO_2 nanoparticles.

The Fourier transform infrared (FTIR) spectra of the pigments and photoelectrodes from anthocyanin, N719, combined anthocyanin-N719, and TiO_2 nanoparticles are shown in Fig. 5. The FTIR spectra of the combined anthocyanin-N719 dye were compared to the infrared spectra of anthocyanin and the N719 standards.[29,52–55] Three vibrational peaks at anthocyanin also appear in the combined anthocyanin-N719. First, the peak presented at 588 cm^{-1} is affected by the stretching vibration of the C–O–C aliphatic ether group from glucose. Second, the peak shown at 1075.1 cm^{-1} is assigned to the in-plane bending vibration of C–H and stretching vibration of C–O. Third, the absorption peak at 1639.2 cm^{-1} is assigned to the stretching vibration of the C=O aromatic group.

Moreover, four vibration peaks at N719 also appear in the combined anthocyanin-N719. First, the peak presented at 663.4 cm^{-1} is affected by the out-of-plane bending vibration of C–H and C–N. Second, the peak shown in the range 670–829 cm^{-1} is assigned to the third-order stretching vibration of C–H and C–N. Third, the absorption peak at 1720.2 cm^{-1} is assigned to the stretching vibration of C=O and COOH groups. Fourth, the peak shown at 2101.1 cm^{-1} is affected by the

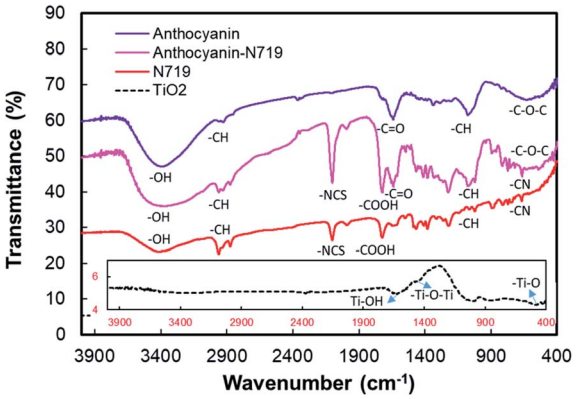

Fig. 5 Fourier transform infrared spectra of anthocyanin, anthocyanin-N719, N719, and TiO_2 nanoparticles.

stretching vibration of the NCS group. The two vibrational peaks also display all the pigments. The vibrational peaks in the range of 2872–2975 cm^{-1} are due to the stretching vibration of the alkane group C–H. The group exists in all the pigments. Finally, the vibrational peak at the range 2975–3600 cm^{-1} is assigned to the stretching vibration of O–H. The group plays an essential role in binding the TiO_2 semiconductors. The vibrational analysis of TiO_2 shows that the first vibration peak at 460.7 cm^{-1} is due to the stretching vibration of –Ti–O. The vibration peaks in the range from 983.5 through 1000.9 cm^{-1} indicate the stretching vibration of Ti–O–Ti. Finally, the vibration peak at 1637.3 cm^{-1} is assigned to the stretching vibration of Ti–OH. Detailed information regarding the vibrational analysis is described in Tables S1 and S2 in the ESI.†

The hydroxyl group is present as the anchoring group, as seen in 2975–3600 cm^{-1} from the vibrational analysis in the anthocyanin as well as the N719 molecules, which facilitates the molecules binding the semiconductor surface. Fig. 6 shows that cyanidin-3-*O*-glucoside possesses eight hydroxyl groups, while N719 contains two carboxylic acid and two carboxylate groups. Thus, it can anchor onto the TiO_2 surface by the close overlap of the ligand π* orbitals and the 3D orbitals of TiO_2. The carboxylic group tends to strengthen the binding by creating a combination of bidentate-bridging and H-bonding involving a donating group from the N719 (and/or Ti–OH) units and an acceptor from the Ti–OH (and/or N719) groups,[56] while the hydroxyl group of anthocyanin results in the monodentate, bridge bidentate, or chelate mode since the first studies reported on anthocyanin DSSCs, while chelate catechol binding has been indicated as the primary and most efficient mode for anthocyanin adsorption on TiO_2.[7,8]

Table 1 tabulates the dye adsorption analysis of anthocyanin, combined anthocyanin-N719, and N719 from UV-Vis analysis following the previous works.[57–61] 'Pre' means pigment absorbance before TiO_2 adsorption, while 'Post' means pigment absorbance after TiO_2 adsorption. From the information based on the dye-adsorption on TiO_2 for anthocyanin, combined

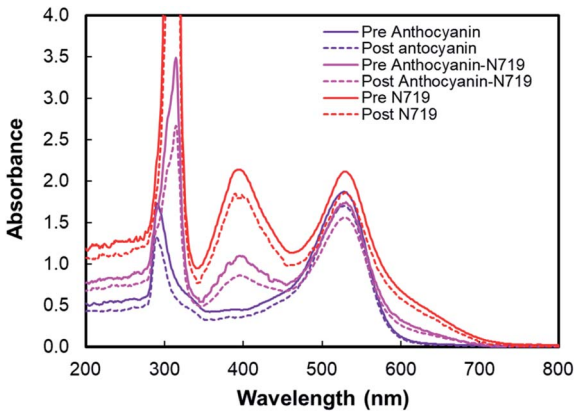

Fig. 7 UV-Vis spectra of anthocyanin, combined anthocyanin-N719, and N719 before and after pigment adsorption onto TiO_2. 'Pre' indicates the absorbance before TiO_2 adsorption while 'Post' indicates the pigment absorbance after TiO_2 adsorption.

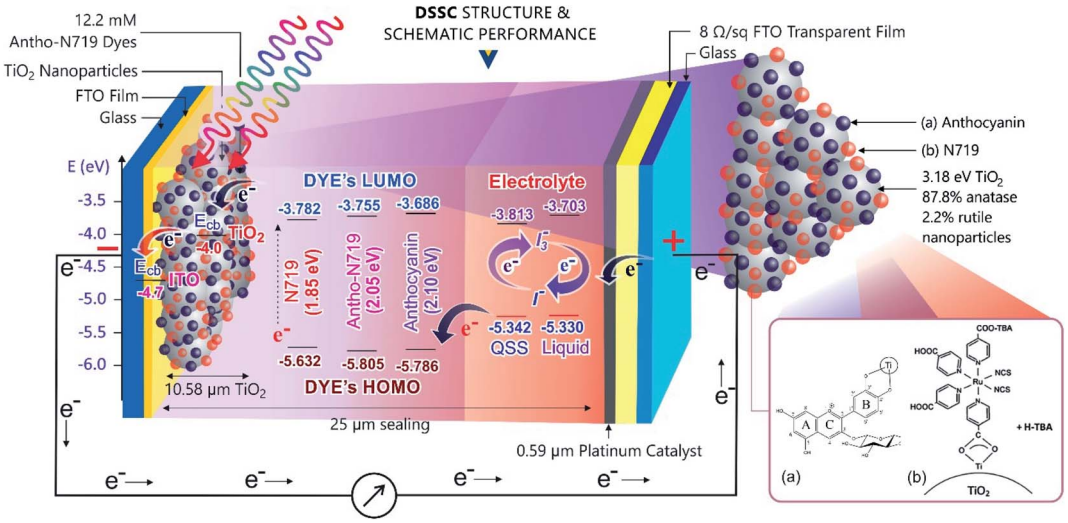

Fig. 6 The DSSC structure and its schematic reaction.

Table 1 Dye adsorption analysis of anthocyanin, combined anthocyanin-N719, and N719 from Fig. 7

Dye	Peak$_1$		Peak$_2$		Peak$_3$		ΔAbs_λ	
	λ_{max} (nm)	Abs (a.u.)	λ_{max} (nm)	Abs (a.u.)	λ_{max} (nm)	Abs (a.u.)	$_{530\ nm}$ (a.u.)	Dye-adsorbed TiO_2 (nmol cm^{-2})
Pre anthocyanin	290	1.727	—	—	528	1.868	0.173	5.657
Post anthocyanin	289	1.328	—	—	529	1.695		
Pre anthocyanin-N719	314	3.486	396	1.098	530	1.744	0.181	6.325
Post anthocyanin-N719	314	2.666	396	0.862	529	1.563		
Pre N719	314	7.000	393	2.139	530	2.116	0.255	7.355
Post N719	314	7.000	395	1.792	530	1.861		

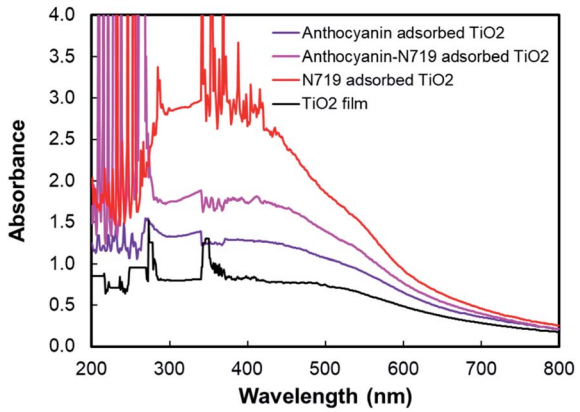

Fig. 8 UV-Vis spectra of anthocyanin-adsorbed TiO_2, combined anthocyanin-N719 adsorbed TiO_2, and N719 adsorbed TiO_2.

anthocyanin-N719, and N719, it was found that the dyes were adsorbed on TiO_2 by 5.657, 6.325, and 7.355 nmol cm^{-2}, respectively. The combination of anthocyanin-N719 (1 : 1) also makes the dye adsorption 11.81% stronger than anthocyanin binding. It can be analyzed that 0.89 nmol N719 and 0.69 nmol anthocyanin dyes were adsorbed on the 0.25 cm^2 TiO_2 nanoparticle film compared to the individual N719 and anthocyanin pigments, which resulted in 1.84 and 1.41 nmol, respectively. These findings were confirmed by the dye-adsorbed TiO_2 absorbance, as seen in Fig. 8. The finding implies that the dye's anchoring group plays a fundamental role in improving the natural pigment's efficiency by strengthening the pigment attachment. The anthocyanin pigment with the carboxylic anchoring group was exciting for further investigation.

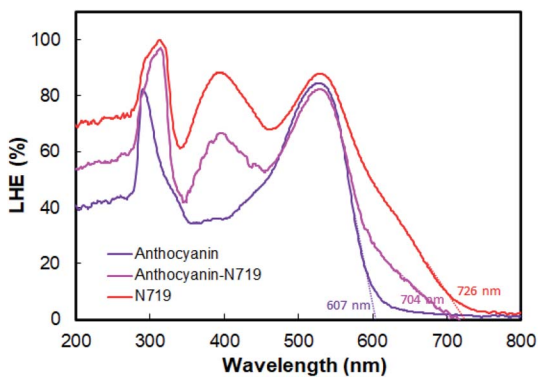

Fig. 9 Light-harvesting efficiency of anthocyanin, combined anthocyanin-N719, and N719 photosensitizers.

Fig. 9 depicts the light-harvesting efficiencies of the pigments. The introduction of N719 into anthocyanin successfully increased the light-harvesting efficiency by 11.2%, as seen in Table 2. Moreover, N719 has 24.5 times better efficiency compared to the anthocyanin dye. The pigment combination successfully reduced the pigment's tail band gap by 0.28 eV. The narrower band gap facilitates better electron transfer. The evidence correlates the dye attachment ability with the presence of many carboxylic groups. It is believed that the bidentate mode of binding is the most effective way of facilitating charge transfers. The middle peak at 395 nm in the combined anthocyanin-N719 pigment appears due to the existence of N719 dye in the combined pigment. The peaks at 395 and 530 nm appear because the low-energy metal-to-ligand charge-transfer transition band exists in N719. During the anthocyanin-N719 combination, the change in the energy of the lowest unoccupied molecular orbital (LUMO) of the N719 ligand causes the π–π* and dπ–π* transitions to occur at higher and lower energies, respectively.[57] As a result, in Table 1, the first peak of anthocyanin has a bathochromic shift of about 24 nm from 290 nm to 314 nm. In the same case, the second peak of anthocyanin has a bathochromic shift of about 1 nm from 528 nm to 529 nm. Moreover, the primary absorption spectra of anthocyanin structure due to the benzoyl (ring A) and cinnamoyl (ring B) systems are identified as Band I (289–300 nm) and Band II (261–266 nm), respectively. Band I shifted due to the presence of a glucose group, showing the absorption spectra in the range of 507–530 nm.[1] We also tested the absorbance spectra of the liquid I^-/I_3^- electrolyte mediator as well as the Pt Film, as seen in Fig. 10. Although this material does not play a significant role in generating electron–hole separation, the result has confirmed that Pt does not significantly absorb the light spectrum within all the UV-Vis range. Moreover, the electrolyte mediator tends to absorb the light spectrum in the range of 220–530 nm. This absorbance range results in the overlap band of I^-/I_3^-, as seen in the usual mechanism of DSSC acting as a redox mediator to regenerate the oxidized dyes. We also summarized the DSSC mechanism based on our investigation in Fig. 6.

Table 2 The analysis of light-harvesting efficiency of anthocyanin, anthocyanin-N719, and N719 dyes

Dye	$LHE_{mean}^{200-500\ nm}$ (%)	λ_{tail} (nm)	$E_{tail\ band\ gap}$ (eV)	$\Delta LHE_{Dye\text{-}Antho}$ (%)
Anthocyanin	54.5	607	2.04	—
Anthocyanin-N719	65.7	704	1.76	11.2
N719	79.0	726	1.70	24.5

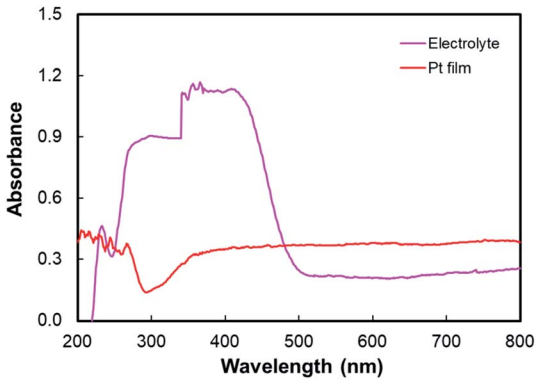

Fig. 10 Absorption spectra of electrolyte I^-/I_3^- and the Pt film.

Fig. 11, 12, and Table 3 show the direct band gaps plotted from the Tauc's plots. The direct band gap corresponds to the vertical electron transition during the excitation.[14] Nguyen showed that a direct band gap transition would dominantly lead to the electron injection process.[58] Therefore, the direct band gap was then investigated to examine the character of the dye's vertical transition during photoexcitation. The electronic structure of the photosensitizers focused on the investigation of anthocyanin, as well as combined anthocyanin-N719 before and after the pigment adsorption. As shown in Fig. 11, anthocyanin, combined anthocyanin-N719, and N719 show a precise fit, resulting in a direct band gap of 2.10, 2.05, and 1.85 eV, respectively. Interestingly, the band gaps decrease since the pigments have been attached to the semiconductor; the direct band gap of anthocyanin, combined anthocyanin-N719, and N719 after adsorption are 1.76, 1.69, and 1.63 eV, respectively, as depicted in Fig. 12. The finding indicates that TiO_2 contributes to the broadening of light absorption, which is consistent with the evidence from Fig. 8. The ruthenium pigment adsorptions contribute to extending the natural pigment photosensitization. Consequently, the pigment lowered the tail band gaps. To find out the exact position of molecular orbital transition, we investigated the HOMO–LUMO level *via* the cyclic voltammetric method, as seen in Fig. 13 and Table 5. The details of the HOMO–LUMO transition have been investigated in our previous work.[1] Although the other level of HOMO–LUMO also contributes to the electronic transitions, the previous work has resulted in the highest electron transition probability of about 49.9%. Table 4 tabulates the HOMO–LUMO level and the gap for the photosensitizer. The LUMO position lowered with the contamination of N719 ($LUMO_{N719}$ < $LUMO_{Anthocyanin\text{-}N719}$ < $LUMO_{Anthocyanin}$). In contrast, the HOMO position decreased with the contamination of anthocyanin ($HOMO_{Anthocyanin}$ < $HOMO_{Anthocyanin\text{-}N719}$ < $HOMO_{N719}$). This finding was confirmed by the previous bathochromic shift of the first peak of anthocyanin in Table 1 and Fig. 7. The pigment shows

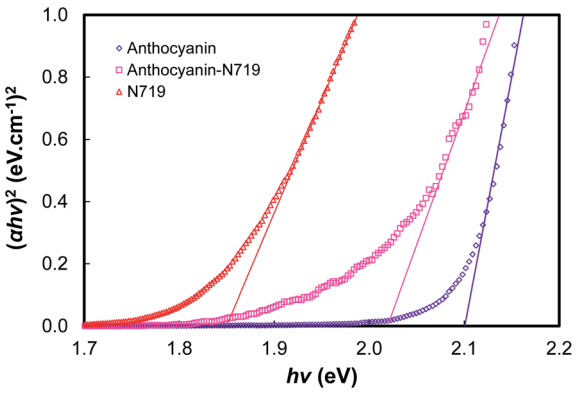

Fig. 11 The plot of $(\alpha hv)^2$ *versus* *hv* for the direct transition of anthocyanin, combined anthocyanin-N719, and N719.

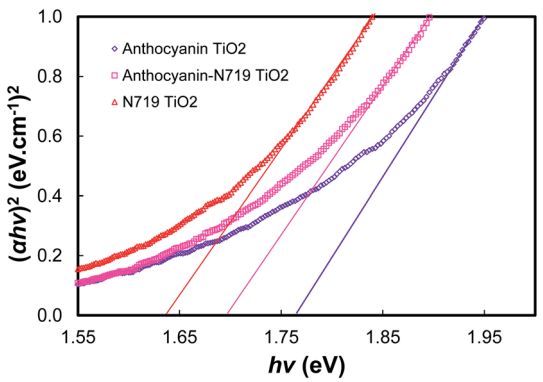

Fig. 12 The plot of $(\alpha hv)^2$ *versus* *hv* for the direct transition of anthocyanin adsorbed TiO_2, combined anthocyanin-N719 adsorbed TiO_2, and N719 adsorbed TiO_2.

Table 3 The band gaps of pigments analyzed from the plot of $(\alpha hv)^2$ *versus* *hv*

Dye	$E_{Band\ Gap}$ (eV)	Dye–TiO_2	$E_{Band\ Gap}$ (eV)
Anthocyanin	2.10	Anthocyanin–TiO_2	1.76
Anthocyanin-N719	2.05	Anthocyanin N719–TiO_2	1.69
N719	1.85	N719–TiO_2	1.63

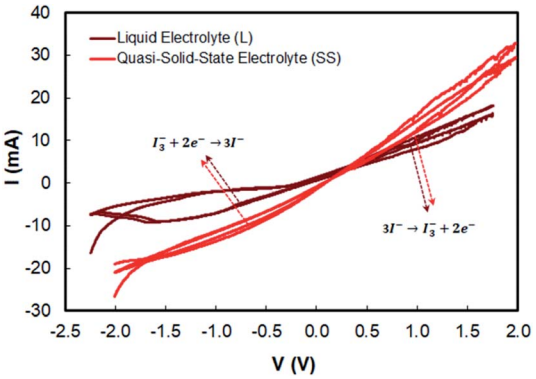

Fig. 13 Cyclic voltammograms of liquid and quasi solid-state electrolytes.

Table 4 The HOMO–LUMO energy levels and band energy gap energies of the dyes

Dye	E_{ox} (V)	E_{HOMO} (eV)	E_{red} (V)	E_{LUMO} (eV)	$E_{Band\ Gap}$ (eV)
Anthocyanin	−1.386	−5.786	−0.714	−3.686	2.10
Anthocyanin-N719	−1.405	−5.805	−0.645	−3.755	2.05
N719	−1.232	−5.632	−0.618	−3.782	1.85

a bathochromic shift of about 24 nm from 290 nm to 314 nm when N719 was introduced into anthocyanin in the combined pigment. In the same case, the second peak of anthocyanin shows a bathochromic shift of about 1 nm from 528 nm to 529 nm. The summary of the HOMO–LUMO levels is illustrated in Fig. 6. It is observed that these findings affect the performance and electron transfer properties of DSSC. The closer the LUMO level to the conduction band of TiO_2, the easier the transfer of the excited electron to the semiconductor. On the other hand, the closer the HOMO position towards the I^- potential, the easier the regeneration of the oxidized dye by the electrons. According to this condition, it is proven explained why N719 has the best performance among the investigated pigments. Interestingly, N719 contamination in anthocyanin results in the lowering of the LUMO level and the raising of the HOMO level. Apart from broadening the pigment's absorption, these levels play a crucial role in facilitating electron transfer. Moreover, the time of electron diffusion and dye regeneration is expected to be the key to improving the stability of natural DSSC in the future.

Based on the intermediate results of optical band gap, LUMO, and HUMO analysis, it is clear that the combination does not significantly exert a good synergetic effect; it seems that the number of individually attached dyes are directly transferred from the electrons to the TiO_2 nanoparticles.

The previous work implied that the novel electrolyte must be introduced into the natural pigment so that the problem of the time for the regeneration of the oxidized dye can be boosted by providing a more stable electrolyte. In this work, we introduce the quasi-solid state electrolyte, which is to be applied to the combined anthocyanin-N719 dye. However, there is a previous exciting discussion regarding the conductivity of quasi-solid state pigments that lowers the cell performance. We believe that a better assembling process also contributes to the attachment of the electrolyte penetrating the semiconductor mesoporous firmly. The better stability of the quasi-solid state electrolyte is also the reason for researchers to fabricate solar cells with more stability.[31,62–67] In this case, by comparing two electrolytes with a similar I^- composition, then considering the dye regeneration by I^- with the mechanism given eqn (4), we can analyze that the quasi-solid state electrolyte presented better dye regeneration due to the 0.012 V lower oxidation potential compared to the liquid electrolyte, resulting in a sharper peak current I_{pc} by about 2.46 mA than that of the liquid electrolyte. As a result, all the dyes have higher open potential voltages by about 0.056, 0.006, and 0.004 V for anthocyanin, combined anthocyanin-N719, and N719, respectively, as tabulated in Table 6. The previous investigation regarding the stability of the dye has been presented by Suyitno.[68] The better electrolyte ability for cycling leads to the reduction and oxidation reaction (I_{pc}/I_{pa} of the quasi-solid state electrolyte < I_{pc}/I_{pa} of liquid electrolyte), resulting in better electrolyte conductivity by about 19.6% based on the analysis from Tables 5, 7, and Fig. 13. This condition is an essential key for stabilizing the dye. The faster electron excitation from the excited dye must be compensated by faster dye regeneration by I^-. Therefore, the condition successfully increased the efficiency of anthocyanin, combined anthocyanin-N719, and N719 based DSSC performance by 0.7, 0.22, and 1.06%, respectively.

Fig. 14 shows the DSSC sensitized by anthocyanin, combined anthocyanin-N719, and N719 with liquid and quasi solid-state electrolytes. The photovoltaic parameters, including short current density (J_{SC}), open-circuit voltage (V_{OC}), fill factor (FF), and power conversion efficiency (η), are tabulated in Table 6. The investigated anthocyanin and N719-based DSSC were

Table 5 Oxidation potentials, reduction potentials, cathodic peak currents I_{pc}, and anodic peak current I_{pa} of liquid and quasi solid-state electrolytes derived using the cyclic voltammetry method

	E_{ox} (V *vs.* Ag/AgCl)	E_{ox} (V)	E_{red} (V *vs.* Ag/AgCl)	E_{red} (V)	ΔE_{red-ox} (V)	I_{pc} (mA)	I_{pa} (mA)	$n = I_{pc}/I_{pa}$
Liquid electrolyte (L)	0.930	−5.330	−0.697	−3.703	−1.627	8.87	5.06	1.753
Quasi-solid state electrolyte (SS)	0.942	−5.342	−0.587	−3.813	−1.529	11.33	8.81	1.286

Table 6 Photovoltaic parameters of DSSC sensitized by anthocyanin, combined anthocyanin-N719, and N719 with liquid and quasi solid-state electrolytes[a]

Dye	Electrolyte	J_{SC} (mA cm^{-2})	V_{OC} (V)	J_{max} (mA cm^{-2})	V_{max} (V)	FF (%)	η (%)	Ref.
Anthocyanin (L)	Liquid	5.69	0.558	4.52	0.431	61.3	1.95	—
Anthocyanin (SS)	Quasi-solid state	6.46	0.614	5.46	0.486	66.7	2.65	—
Anthocyanin-N719 (L)	Liquid	8.25	0.615	5.45	0.468	64.9	3.29	—
Anthocyanin-N719 (SS)	Quasi-solid state	12.66	0.621	7.47	0.470	44.6	3.51	—
N719 (L)	Liquid	16.01	0.647	13.86	0.465	62.2	6.45	—
N719 (SS)	Quasi-solid state	20.78	0.651	15.71	0.478	55.5	7.51	—
Hesperidin[c]	Liquid	3.23	0.480	2.16	0.320	45.0	0.71	2
C3G + P3G[b]	Liquid	5.46	0.523	4.69	0.449	74.0	2.08	1
Unpurified black rice[d]	Liquid	5.44	0.550	4.67	0.473	74.0	2.17	4

[a] This work employed TiO_2 (nanoparticles, 19.18 nm, 50.99 m^2 g^{-1} surface area, 87.8% anatase 12.2% rutile, 10.58 μm thickness, 3.18 eV band gap) – combined purified anthocyanin-N719 (12.2 mM, pH 1.0) – I^-/I_3^- with liquid electrolyte (containing lithium iodide (0.1 M)/Iodine (0.050 M) in acetonitrile and 0.6 M 1-buty-3-methylimidazolium iodide (BMII) and 0.5 M 4-*tert*-butylpyridine (TBP), + polyethylene oxide (MW = 1×10^6) for quasi-solid state phase) – Pt and 25 μm sealing thickness. [b] TiO_2 (nanoparticles, 13 nm, 120 m^2 g^{-1} surface area, 100% anatase, 7.3 μm thickness, 3.2 eV band gap) – unpurified pigment with chlorophyll *b* copigment (1.92 mM, pH 7.0) – I^-/I_3^- with liquid electrolyte (containing tetrabutylammonium iodide (0.5 M)/iodine (0.05 M) in acetonitrile and 70 mM *tert*-butylpyridine, 0.1 M lithium iodide, and 35 mM pyridine) – Pt and 50 μm sealing thickness. [c] TiO_2 (nanoparticles, 20.47 nm, 52 m^2 g^{-1} surface area, mixed 70% anatase 30% rutile, 11.06 μm thickness, 3.2 eV band gap) – double anthocyanin pigments (2.00 mM, pH 2.0) – I^-/I_3^- with liquid electrolyte (containing lithium iodide (0.1 M)/iodine (0.05 M) in acetonitrile and 0.6 M 1-buty-3-methylimidazolium iodide (BMII) and 0.5 M 4-*tert*-butylpyridine (TBP)) – Pt and 25 μm sealing thickness. [d] TiO_2 (nanoparticles, 13 nm, 120 m^2 g^{-1} surface area, 100% anatase, 7.3 μm thickness, 3.2 eV band gap) – unpurified pigment with chlorophyll *b* copigment (1.92 mM, pH 7.0) – I^-/I_3^- with liquid electrolyte (containing tetrabutylammonium iodide (0.5 M)/iodine (0.05 M) in acetonitrile and 70 mM *tert*-butylpyridine, 0.1 M lithium iodide, and 35 mM pyridine) – Pt and 50 μm sealing thickness.

Table 7 Electrochemical impedance spectroscopy parameters obtained by fitting the Nyquist plots with the equivalent circuit in Fig. 15b for DSSC. The details of the calculation method can be seen in ESI

Dye	R_d (Ω)	R_r (Ω)	R_{pt} (Ω)	τ_d (μs)	τ_n (ms)	L_n (μm)	D_n 10^{-3} (cm^2 s^{-1})	$C_{\mu_{elec}}$ (μF)	σ_n 10^{-4} (S m^{-1})	η (%)	Ref.
Anthocyanin L	2.53	96.18	6.97	33.30	13.55	65.23	33.58	140.86	16.73	1.95	—
Anthocyanin S	2.10	81.18	6.50	31.00	13.27	65.78	36.12	163.45	20.15	2.65	—
Anthocyanin-N719 L	1.78	64.49	4.81	28.10	1.71	63.68	39.82	264.49	23.78	3.29	—
Anthocyanin-N719 S	1.58	58.53	4.41	26.50	1.67	64.39	42.27	285.43	26.78	3.51	—
N719 L	1.00	43.40	2.70	23.40	1.05	69.70	47.74	242.84	42.32	6.45	—
N719 S	0.90	38.41	2.46	21.00	1.03	69.12	53.22	267.48	47.02	7.51	—
Hesperidin	13.60	265.00	—	220.00	4.29	32.20	2.56	15.20	7.14	0.71	2
C3G + P3G	0.90	73.32	25.07	25.07	1.03	—	21.30	14.09	10.8	2.08	1
Unpurified black rice	21.90	281.60	—	70.92	3.63	28.6	16.96	14.32	—	2.17	4

compared to the combined anthocyanin-N719 DSSC. The result shows that the N719 dye-sensitized solid-state solar cell with 7.51% efficiency is superior to the other dyes. The photocurrent density, open-circuit voltage, fill factor, and overall cell efficiency of the N719 dye were observed to be 20.78 mA cm^{-2}, 0.651 V, 0.55, and 7.51%, respectively. All the quasi-solid state dye-sensitized solar cells resulted in better performance than the liquid-based dye-sensitized solar cells by about 0.70, 0.22, and 1.06% for anthocyanin, anthocyanin-N719, and N719, respectively. The lower oxidation potential of the quasi-solid state electrolyte by about 0.012 V contributes to the broader open-circuit voltages of anthocyanin, anthocyanin-N719, and N719 by about 0.056, 0.006, and 0.004 V, respectively. The combination of lower LUMO gaps of anthocyanin-N719 and N719 of about 0.069 and 0.096 eV, respectively, towards anthocyanin's LUMO with a broader dye absorbance of anthocyanin-N719 and N719 of 11.2 and 24.5%, respectively, contribute to higher short current densities of anthocyanin-N719 and N719 by about 2.56–6.20 and 10.32–14.32 mA cm^{-2}, respectively, for liquid and quasi solid-state DSSCs. Although the tendency of changes in the fill factor due to the change in the total internal resistance of DSSC has not been found, the

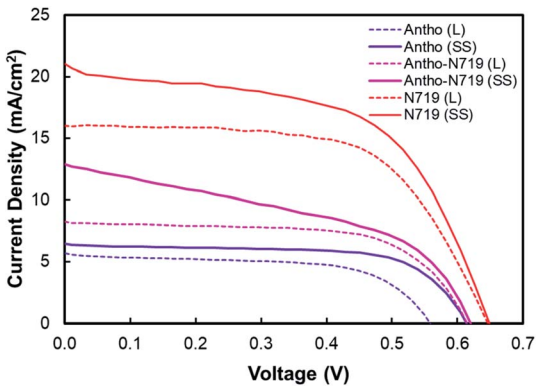

Fig. 14 *I–V* curve of DSSC sensitized by anthocyanin, combined anthocyanin-N719, and N719 with liquid and quasi solid-state electrolytes.

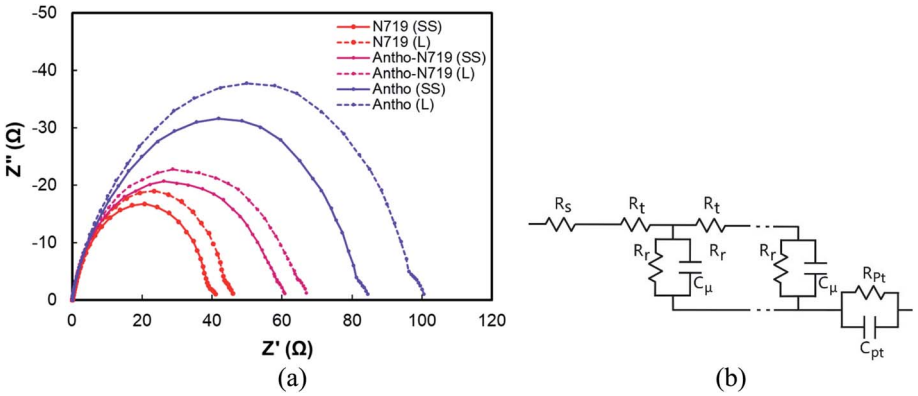

Fig. 15 (a) Nyquist plots of DSSC sensitized by anthocyanin, combined anthocyanin-N719, and N719 with liquid and quasi-solid state electrolytes, (b) illustration of the equivalent circuit elements showing the diffusion-recombination transmission line under reflecting boundary conditions fit that overlays a highly idealized photoanode schematic at various potentials in the dark.

stronger pigment adsorptions of anthocyanin-N719 and N719 by about 0.668 and 1.698 nmol cm^{-2} towards anthocyanin on the TiO_2 semiconductor due to the presence of hydroxyl, carboxyl, and carbonyl groups is also an essential factor facilitating faster electron transfer.

Fig. 15(a) shows the Nyquist plot of DSSC sensitized by anthocyanin, combined anthocyanin-N719, and N719 with liquid and quasi solid-state electrolytes. At the same time, Fig. 15(b) illustrates that the equivalent circuit elements showing the diffusion-recombination transmission line under reflecting boundary conditions fit overlays a highly idealized photoanode schematic at various potentials in the dark. Based on the EIS investigation, this evidence has been shown in Table 7 for the analysis of diffusion time. Anthocyanin-N719 and N719 are 4.5–5.2 μs and 9.9–10 μs faster than anthocyanin DSSC for both liquid and quasi-solid state electrolytes, respectively. The lower oxidation potential of the quasi-solid state electrolyte shortened the regeneration time by 0.28, 0.04, and 0.02 ms for anthocyanin, combined anthocyanin-N719, and N719 pigments. The table also presents that the faster the electron transfer, the higher the conductivity of the pigment; thus, the greater the cell performance. The lower the electrolyte oxidation potential towards HOMO, the wider the open-circuit voltage of cells. These findings are also supported by the tendency of electrolyte chemical capacitance enhancements.

To strengthen our findings towards our previously published works,[1,2,12,14,60,69] we strengthen our findings as to the state of the art of the engineering of black rice-based anthocyanin pigments. To the best of our knowledge, this work has achieved the highest efficiency of anthocyanin dye-sensitized quasi-solid state solar cells of 2.65%. The analysis of the absorbance, the adsorption, the HOMO–LUMO level, and the electron transfer play essential roles in determining and comparing anthocyanin with the standardized N719 pigment. There is no previous work reporting the details of the head-to-head performance of natural and synthetic pigments, considering the above-mentioned parameters. The dye combination of anthocyanin-N719 successfully improved the performance of both liquid and quasi-solid state anthocyanin dye-sensitized solar cells by about 1.34 and 0.86%, respectively. Regardless of the DSSC structures, which have been investigated previously, compared to the previously investigated anthocyanin-based dye, the result presents superior performance among them. This improvement is significantly affected by the enhancement in the short circuit photocurrent density due to the dye's higher concentration and faster-oxidized dye regeneration. Other dye considerations such as pH, dye attachment, HOMO–LUMO, co-sensitization, purification, and the chemical structure of D–π–A also contribute to the final performance of the DSSC. As tabulated in Table 7, the condition of the EIS tests, such as applying forward bias or placing the cell under irradiation, will significantly affect the diffusion resistance, recombination resistance, and the ratio between them. The table shows that this work has obtained a better diffusion rate with a range of $(33.58–53.22) \times 10^{-3}$ cm^2 s^{-1} as well as better conductivity with a range of $(16.73–47.02) \times 10^{-4}$ S m^{-1}. The condition leads to verifying the better performance of the cells.

4. Conclusions

The natural pigment was modified to improve the cell performance by modifying the D–π–A structure. Interestingly, in comparison with N719, the molar extinction coefficient of anthocyanin dye is 26 900 M^{-1} cm^{-1} at 550 nm, whereas that of the N719 photosensitizer is 14 000 M^{-1} cm^{-1} at 515 nm. By investigating and comparing these pigments, we believe that the finding will contribute to the development of novel modified natural photosensitizer pigments for future natural dye-sensitized solar cells. Moreover, the quasi-solid state electrolyte introduced in this work also presents a better performance of the photosensitizer compared to the liquid-based electrolyte.

The combination of anthocyanin-N719 (1 : 1) improved the dye adsorption by making it 11.81% stronger than anthocyanin binding. The pigment combination successfully enhanced the absorbance of anthocyanin adsorbed on TiO_2 by 38.0%. At the same time, the pigment combination decreased the N719 adsorbed TiO_2 by about 32.4%. Interestingly, the N719 contamination in the anthocyanin results in the lowering of the

LUMO level and the raising of the HOMO level. The combination of lower LUMO gaps of anthocyanin-N719 and N719 of 0.069 and 0.096 eV, respectively, towards anthocyanin's LUMO with a broader dye absorbance of anthocyanin-N719 and N719 by about 11.2 and 24.5%, respectively. As a consequence, the cell shows a better diffusion rate with the range 33.58–53.22 $\times$ 10^{-3} cm^2 s^{-1} as well as better conductivity with the range of 16.73–47.02 $\times$ 10^{-4} S m^{-1}, leading to the verification of the better performance of the cells. A quasi-solid state electrolyte with the combined anthocyanin-ruthenium dye-sensitized solar cell achieved 3.51%. The work also obtained the highest anthocyanin dye-sensitized quasi-solid state solar cell efficiency of 2.65%.

In terms of the quasi-solid state electrolyte investigation, it has presented better dye regeneration due to the 0.012 V lower oxidation potential compared to that of the liquid electrolyte, resulting in a stronger peak current I_{pc} by about 2.46 mA than that of the liquid electrolyte. As a result, all the dyes have higher open potential voltages by about 0.056, 0.006, and 0.004 V for anthocyanin, combined anthocyanin-N719, and N719, respectively. The better the electrolyte ability for cycling the reduction and oxidation reaction (I_{pc}/I_{pa} of the quasi-solid state electrolyte < I_{pc}/I_{pa} of the liquid electrolyte), the better the electrolyte conductivity, which is about 19.6% better. The faster electron excitation from the excited dye must be compensated by faster dye regeneration by I^-. Therefore, the condition successfully increased the efficiency of anthocyanin, combined anthocyanin-N719, and N719-based DSSC by about 0.7, 0.22, and 1.06%, respectively.

The finding implies that the dye's anchoring group plays a fundamental role in improving the natural pigment efficiency by strengthening the pigment attachment. The anthocyanin pigment with carboxylic anchoring groups is exciting for further investigation.

Conflicts of interest

There are no conflicts of interest to declare.

Acknowledgements

This work was supported by the Program Penelitian Kolaborasi Indonesia, 2020 (Grant Number 924 /UN40.D/PT/2020). Moreover, this work was also partially supported by Indonesia Ministry of Education and Culture, and Indonesia Ministry of Research and Technology under grant scheme of World Class University Program managed by Institut Teknologi Bandung.

References

1 E. C. Prima, A. Nuruddin, B. Yuliarto, G. Kawamura and A. Matsuda, *New J. Chem.*, 2018, **42**, 11616–11628.
2 E. C. Prima, N. N. Hidayat, B. Yuliarto, Suyatman and H. K. Dipojono, *Spectrochim. Acta Mol. Biomol. Spectrosc.*, 2017, **171**, 112–125.
3 G. Calogero, A. Bartolotta, G. Di Marco, A. Di Carlo and F. Bonaccorso, *Chem. Soc. Rev.*, 2015, **44**, 3244–3294.
4 Y. Ooyama and Y. Harima, *Eur. J. Org. Chem.*, 2009, **2009**, 2903–2934.
5 B. O'Regan and M. Grätzel, *Nature*, 1991, **353**, 737–740.
6 Z.-S. Wang, H. Kawauchi, T. Kashima and H. Arakawa, *Coord. Chem. Rev.*, 2004, **248**, 1381–1389.
7 J. Luo, Z. Wan, C. Jia, Y. Wang, X. Wu and X. Yao, *Electrochim. Acta*, 2016, **211**, 364–374.
8 P. Sharma, I. Sharma and S. C. Katyal, *J. Appl. Phys.*, 2009, **105**, 053509.
9 S. A. Sapp, C. M. Elliott, C. Contado, S. Caramori and C. A. Bignozzi, *J. Am. Chem. Soc.*, 2002, **124**, 11215–11222.
10 F. Kabir, M. M. H. Bhuiyan, M. S. Manir, M. S. Rahaman, M. A. Khan and T. Ikegami, *Results Phys.*, 2019, **14**, 102474.
11 W. Ghann, H. Kang, T. Sheikh, S. Yadav, T. Chavez-Gil, F. Nesbitt and J. Uddin, *Sci. Rep.*, 2017, **7**, 41470.
12 E. C. Prima, B. Yuliarto, V. Suendo and Suyatman, *J. Mater. Sci.: Mater. Electron.*, 2014, **25**, 4603–4611.
13 S. Nakade, Y. Saito, W. Kubo, T. Kitamura, Y. Wada and S. Yanagida, *J. Phys. Chem. B*, 2003, **107**, 8607–8611.
14 E. C. Prima, M. Qibtiya, B. Yuliarto, Suyatman and H. K. Dipojono, *Ionics*, 2016, **22**, 1687–1697.
15 N. Lahmer, N. Belboukhari, A. Cheriti and K. Sekkoum, *Der Pharma Chem.*, 2015, **7**, 1–4.
16 C.-Y. Chien and B.-D. Hsu, *Sol. Energy*, 2013, **98**, 203–211.
17 N. Anuar, A. F. Mohd Adnan, N. Saat, N. Aziz and R. Mat Taha, *Sci. World J.*, 2013, **2013**, 10.
18 A. Ordaz-Galindo, P. Wesche-Ebeling, R. E. Wrolstad, L. Rodriguez-Saona and A. Argaiz-Jamet, *Food Chem.*, 1999, **65**, 201–2016.
19 N. T. R. N. Kumara, P. Ekanayake, A. Lim, L. Y. C. Liew, M. Iskandar, L. C. Ming and G. K. R. Senadeera, *J. Alloys Compd.*, 2013, **581**, 186–191.
20 Y. Duan, Q. Tang, Y. Chen, Z. Zhao, Y. Lv, M. Hou, P. Yang, B. He and L. Yu, *J. Mater. Chem. A*, 2015, **3**, 5368–5374.
21 Y. Yang, C.-h. Zhou, S. Xu, H. Hu, B.-l. Chen, J. Zhang, S.-j. Wu, W. Liu and X.-z. Zhao, *J. Power Sources*, 2008, **185**, 1492–1498.
22 Y. Kimura, T. Maeda, S. Iuchi, N. Koga, Y. Murata, A. Wakamiya and K. Yoshida, *J. Photochem. Photobiol., A*, 2017, **335**, 230–238.
23 K. Kalyanasundaram and M. Grätzel, *Coord. Chem. Rev.*, 1998, **177**, 347–414.
24 S. Akın, S. Açıkgöz, M. Gülen, C. Akyürek and S. Sönmezoğlu, *RSC Adv.*, 2016, **6**, 85125–85134.
25 G. Calogero, I. Citro, G. Di Marco, S. Caramori, L. Casarin, C. A. Bignozzi, J. Avó, A. Jorge Parola and F. Pina, *Photochem. Photobiol. Sci.*, 2017, **16**, 1400–1414.
26 M. A. M. Al-Alwani, H. Abu Hasan, N. Kaid Nasser Al-Shorgani and A. B. S. A. Al-Mashaan, *Mater. Chem. Phys.*, 2020, **240**, 122204.
27 J. M. Cole, G. Pepe, O. K. Al Bahri and C. B. Cooper, *Chem. Rev.*, 2019, **119**, 7279–7327.
28 Y. Chiba, A. Islam, Y. Watanabe, R. Komiya, N. Koide and L. Han, *Jpn. J. Appl. Phys.*, 2006, **45**, L638.
29 A. Versari, R. Boulton and J. Thorngate, in *Red Wine Color*, American Chemical Society, 2004, vol. 886, ch. 5, pp. 53–67.
30 Y. Liu and J. Wang, *Thin Solid Films*, 2010, **518**, e54–e56.

31 A. A. Mohamad, *J. Power Sources*, 2016, **329**, 57–71.
32 J. H. Yang, C. W. Bark, K. H. Kim and H. W. Choi, *Materials*, 2014, **7**, 3522–3532.
33 Y. S. Park, S. J. Kim and H. I. Chang, *Korean J. Microbiol. Biotechnol.*, 2008, **36**, 55–60.
34 G. R. Takeoka, L. T. Dao, H. Tamura and L. A. Harden, *J. Agric. Food Chem.*, 2005, **53**, 4932–4937.
35 S. N. Ryu, S. J. Han, S. Z. Park and H. Y. Kim, *Korean J. Crop. Sci.*, 2000, **45**, 257–260.
36 S. Y. Chae, M. K. Park, S. K. Lee, T. Y. Kim, S. K. Kim and W. I. Lee, *Chem. Mater.*, 2003, **15**, 3326–3331.
37 B. Tryba, M. Tygielska, C. Colbeau-Justin, E. Kusiak-Nejman, J. Kapica-Kozar, R. Wróbel, G. Żołnierkiewicz and N. Guskos, *Mater. Res. Bull.*, 2016, **84**, 152–161.
38 J. H. Lee, *Food Sci. Biotechnol.*, 2010, **19**, 391–397.
39 A. G. Al-Sehemi, A. Irfan and A. M. Fouda, *Spectrochim. Acta, Part A*, 2013, **111**, 223–229.
40 A. Fernandes, G. Ivanova, N. F. Brás, N. Mateus, M. J. Ramos, M. Rangel and V. de Freitas, *Carbohydr. Polym.*, 2014, **102**, 269–277.
41 J. L. Bredas, R. Silbey, D. S. Boudreaux and R. R. Chance, *J. Am. Chem. Soc.*, 1983, **105**, 6555–6559.
42 J. Tauc, R. Grigorovici and A. Vancu, *Phys. Status Solidi B*, 1966, **15**, 627–637.
43 M. Grätzel, *J. Photochem. Photobiol., C*, 2003, **4**, 145–153.
44 Q. Wang, J.-E. Moser and M. Grätzel, *J. Phys. Chem. B*, 2005, **109**, 14945–14953.
45 J. Bisquert, *J. Phys. Chem. B*, 2004, **108**, 2323–2332.
46 J. Bisquert, G. Garcia-Belmonte and Á. Pitarch, *ChemPhysChem*, 2003, **4**, 287–292.
47 J. Bisquert, *Phys. Chem. Chem. Phys.*, 2003, **5**, 5360–5364.
48 J. Bisquert and V. S. Vikhrenko, *Electrochim. Acta*, 2002, **47**, 3977–3988.
49 J. Bisquert, *J. Phys. Chem. B*, 2002, **106**, 325–333.
50 J. Bisquert and A. Compte, *J. Electroanal. Chem.*, 2001, **499**, 112–120.
51 B. Yuliarto, W. Septina, K. Fuadi, F. Fanani, L. Muliani and Nugraha, *Adv. Mater. Sci. Eng.*, 2010, **2010**, 6.
52 L. K. Singh, T. Karlo and A. Pandey, *Spectrochim. Acta, Part A*, 2014, **118**, 938–943.
53 K. E. Lee, M. A. Gomez, S. Elouatik, G. B. Shan and G. P. Demopoulos, *J. Electrochem. Soc.*, 2011, **158**, H708–H714.
54 A. Jantasee, K. Thumanu, N. Muangsan, W. Leeanansaksiri and D. Maensiri, *Food Anal. Methods*, 2014, **7**, 389–399.
55 A. Soriano, P. M. Pérez-Juan, A. Vicario, J. M. González and M. S. Pérez-Coello, *Food Chem.*, 2007, **104**, 1295–1303.
56 K. E. Lee, M. A. Gomez, S. Elouatik and G. P. Demopoulos, *Langmuir*, 2010, **26**, 9575–9583.
57 P. Wen, Y. Han and W. Zhao, *Int. J. Photoenergy*, 2012, **2012**, 7.
58 V.-H. Nguyen, H.-Y. Chan and J. C. S. Wu, *J. Chem. Sci.*, 2013, **125**, 859–867.
59 E. C. Prima, B. Yuliarto, Suyatman and H. K. Dipojono, *Mater. Sci. Forum*, 2017, **889**, 178–183.
60 M. A. Qibtiya, E. C. Prima, B. Yuliarto and Suyatman, *Mater. Sci. Forum*, 2016, **864**, 154–158.
61 E. C. Prima, B. Yuliarto, Suyatman and H. K. Dipojono, *J. Phys.: Conf. Ser.*, 2016, **739**, 012031.
62 M. Suzuka, N. Hayashi, T. Sekiguchi, K. Sumioka, M. Takata, N. Hayo, H. Ikeda, K. Oyaizu and H. Nishide, *Sci. Rep.*, 2016, **6**, 28022.
63 L. Tao, Z. Huo, Y. Ding, Y. Li, S. Dai, L. Wang, J. Zhu, X. Pan, B. Zhang, J. Yao, M. K. Nazeeruddin and M. Grätzel, *J. Mater. Chem. A*, 2015, **3**, 2344–2352.
64 T. S. Senthil, N. Muthukumarasamy, D. Velauthapillai, S. Agilan, M. Thambidurai and R. Balasundaraprabhu, *Renewable Energy*, 2011, **36**, 2484–2488.
65 H. Yang, M. Huang, J. Wu, Z. Lan, S. Hao and J. Lin, *Mater. Chem. Phys.*, 2008, **110**, 38–42.
66 J. Wu, Z. Lan, D. Wang, S. Hao, J. Lin, Y. Huang, S. Yin and T. Sato, *Electrochim. Acta*, 2006, **51**, 4243–4249.
67 E. Stathatos, P. Lianos, S. M. Zakeeruddin, P. Liska and M. Grätzel, *Chem. Mater.*, 2003, **15**, 1825–1829.
68 S. Suyitno, T. J. Saputra, A. Supriyanto and Z. Arifin, *Spectrochim. Acta Mol. Biomol. Spectrosc.*, 2015, **148**, 99–104.
69 E. Cahya Prima, B. Yuliarto and H. Kresno Dipojono, *Adv. Mater. Res.*, 2015, **1112**, 317–320.

